Effect of wind on continental shelf carbon fluxes off southeast Australia: A numerical model

Helen S. Macdonald,[1] Mark E. Baird,[1] and Jason H. Middleton[1,2]

[1] A coupled physical-biological-chemical model is used to study the effect of upwelling-favorable and downwelling-favorable winds on carbon biogeochemistry on the continental shelf off the southeast Australian mainland. Along the continental shelf, from 30°S to 34°S, upwelling-favorable winds, with the aid of bottom Ekman transport, bring dissolved-inorganic-carbon (DIC)-rich slope waters onto the shelf, increasing the carbon held in shelf waters. For downwelling-favorable winds, bottom Ekman transport still lifts slope waters onto the shelf, but the slope water transport, and therefore carbon held, is reduced compared with the upwelling scenario. Under upwelling-favorable winds, filaments of DIC and dissolved-inorganic-nitrogen (DIN)-rich water reaching the surface produce an outgassing near the site of upwelling and absorption downstream due to primary productivity. In a region of the ocean that is generally absorbing, the net effect of upwelling is a reduced absorption of atmospheric CO_2 as a result of the ratio of deep DIC and DIN (12.2:1 mol C:mol N) being greater than the Redfield ratio (6.625). Carbon fluxes in the waters off the southeast Australian mainland are variable in space, with the transport of continental shelf waters to deep waters occurring mainly where alongshore currents separate from the coast and flow over the 200-m isobath.

1. Introduction

[2] The oceanic sink for atmospheric carbon has been estimated to be 2.0 ± 0.4 Gt C yr^{-1} [*Takahashi et al.*, 2002; *McNeil et al.*, 2003], or approximately a third of the global anthropogenic carbon emissions. The Tasman Sea is an area of the global ocean that is generally absorbing [*Takahashi et al.*, 2002] as result of surface partial pressure of CO_2, pCO_2, being less than the present atmosphere values.

[3] The regions of greatest uncertainty in estimating air-sea fluxes of carbon are the continental shelves [*Yool and Fasham*, 2001]. Whether a particular continental shelf is a source or sink of carbon, and the strength of the cross-shelf exchange, will depend on factors such as shelf morphology, ocean circulation and temperature, biological processes as well as the nature of terrestrial inputs [*Cai et al.*, 2006]. Some shelves can vary between absorbing and outgassing carbon dioxide through the annual cycle, or as a function of regional transient features such as local winds and currents [*Shim et al.*, 2007]. In order to understand the air-sea and cross-shelf carbon fluxes on a particular continental shelf, local physical, biological and chemical processes must be quantified [*Tsunogai et al.*, 1999; *Borges et al.*, 2005; *Cai et al.*, 2006].

[4] The New South Wales (NSW) continental shelf lies along the eastern seaboard of the Australian continent from 28.4°S to 37.5°S (Figure 1). Because of the dry climate and relatively small catchment area of the eastern seaboard, there is little river/estuarine discharge of nitrogen along the southeast Australian coastline. As such, the main source of nitrogen for phytoplankton growth is dissolved-inorganic-nitrogen (DIN) upwelled from the lower oceanic layers [*Pritchard et al.*, 1997].

[5] Physical and biological processes on the NSW continental shelf are dominated by the presence of the East Australian Current (EAC), a poleward flowing western boundary current [*Godfrey et al.*, 1980]. The evolution of the EAC can be described in four distinct stages [*Ridgway and Dunn*, 2003]: the current forms between 15°S and 24°S, intensifies between 22°S and the point of separation from the continental shelf as the shelf narrows, separates from the coast between 30°S and 31°30′S, and, for the portion of the EAC that remains connected to the coast, a current of declining strength is seen through to 43°S (Figure 2 shows the current fields used in this paper with EAC separation around 30°S).

[6] *Roughan and Middleton* [2002, 2004] identified a number of upwelling mechanisms off the NSW coast: wind-driven upwelling, upwelling driven by the encroachment of the EAC onto the continental shelf, acceleration of the current resulting from the narrowing of the continental shelf at Smoky Cape (31°S, Figure 1), and the separation of

---

[1]Climate and Environmental Dynamics Laboratory, School of Mathematics and Statistics, University of New South Wales, Sydney, New South Wales, Australia.

[2]Department of Aviation, University of New South Wales, Sydney, New South Wales, Australia.
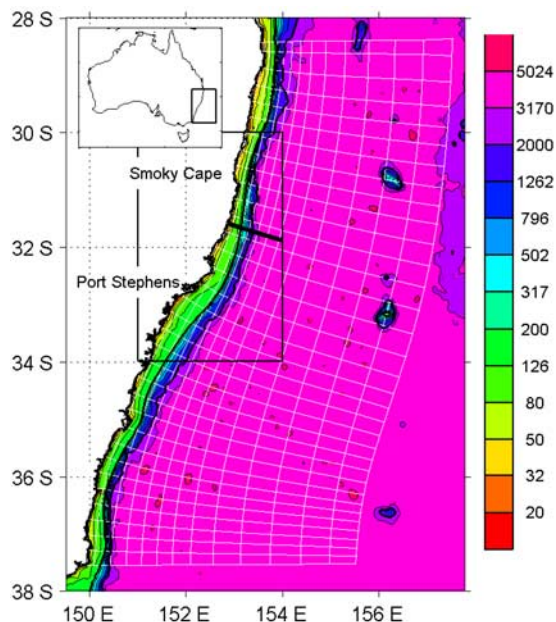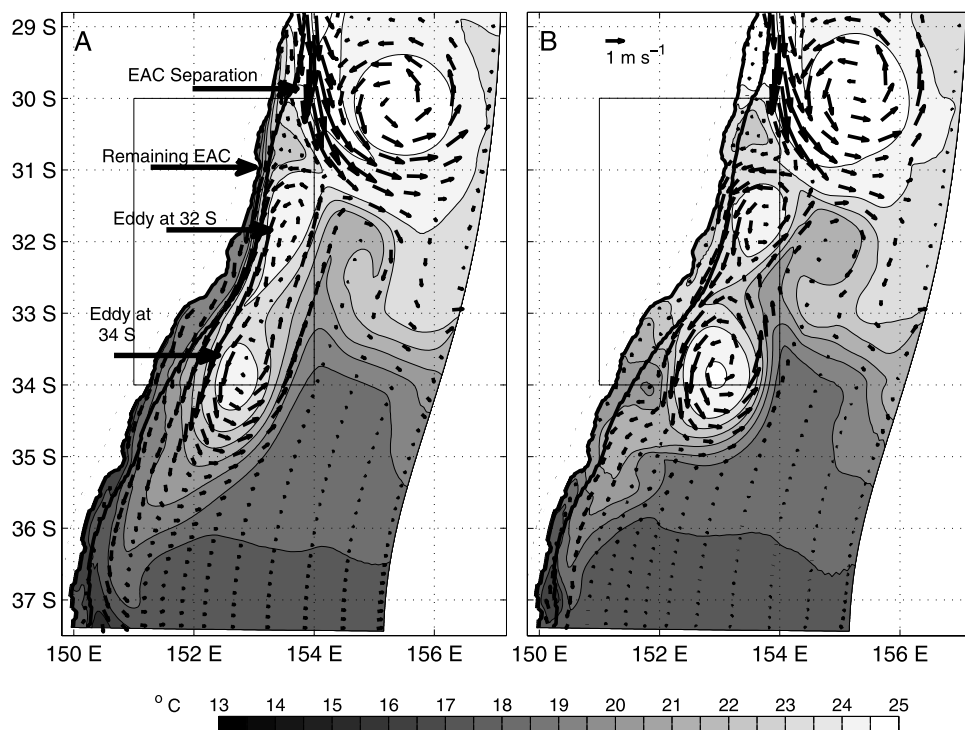
Figure 1. The model configuration. The inset shows the location of the study region off the coast of southeast Australia. The larger panel shows the outer grid lines and every 10th line within the domain. A high-resolution coastline is shown in black. The color scale shows a 2′ bathymetry used to calculate model depth. The 200-m and 2000-m isobaths are shown with thicker black contour lines. The boxed area shows the region plotted in Figures 3, 5, 7, 8, 9, 10, and 14. The slice for Figures 4 and 6 is along the thick black line within the boxed area.

the EAC from the coast. The upwelling associated with these mechanisms produces a strong biological response [*Hallegraeff and Jeffery*, 1993], especially immediately poleward and downstream from the separation point [*Ajani et al.*, 2001; *Oke and Middleton*, 2001; *Baird et al.*, 2007].

[7] In recent work, a coupled physical-biological model of the waters off the NSW coast was used to investigate the biological response to wind-forced and current-driven upwelling [*Baird et al.*, 2006a, 2006b]. The cross-shelf fluxes of nitrogen (composed of dissolved-inorganic-nitrogen, DIN, and phytoplankton and zooplankton biomass) were quantified by *Baird et al.* [2006b, section 5.2]. A comparison of idealized 20-day northerly and southerly wind scenarios demonstrated greater accumulation of total nitrogen on the continental shelf of the northerly winds scenario as a result of (1) a greater inflow of DIN at depth on the northern boundary, and (2) a reduced net offshore transport of DIN. The reduced offshore DIN transport occurred because the DIN brought onto the shelf at depth was greater than the DIN, phytoplankton and zooplankton biomass lost to the open ocean in the surface cross-shelf transport. In contrast, the offshelf organic matter flux (sum of phytoplankton and zooplankton biomass) was greater for the northerly wind simulation than the southerly wind simulation (2 Gg N d^{-1} compared to 0.9 Gg N d^{-1}).

[8] *Baird et al.* [2006b] also investigated the spatial variability in nitrogen fluxes along the continental shelf break (200-m isobath). The offshelf organic matter flux was situated higher in the water column in the northerly wind simulation than the southerly simulation. Both simulations showed regions of onshelf and offshelf transport of DIN,

Figure 2. The sea surface temperature (gray scale) and surface velocity field (arrows) averaged from day 10 to 20 for (a) the upwelling wind scenario and (b) the downwelling wind scenario. The thick arrows identify significant features in the flow field, and a box encloses the study region. The 200-m isobath is shown as a solid line.

phytoplankton and zooplankton, a result of the spatial variability of the flow over the 200-m isobath. In particular, there was strong offshelf transport at 31°S–33°S due to the separation of the EAC, and generally onshelf transport south of 34°S.

[9] The model of *Baird et al.* [2006b] only considered nitrogen fluxes, the limiting nutrient of the region [*Pritchard et al.*, 1997]. In order to estimate carbon fluxes, the model of *Baird et al.* [2006b] has been enhanced through the addition of: (1) a detrital state variable and the processes of detrital particulate sinking and remineralization of phytoplankton and zooplankton through detritus to DIN; (2) a carbon chemistry model based on the Ocean-Carbon Cycle Model Intercomparison Project (OCMIP) numerical methods that considers the dynamics of dissolved-inorganic-carbon (DIC) and total alkalinity and implements wind-speed-dependent air-sea fluxes [*Najjar and Orr*, 1999]; (3) an improved alongshore spatial resolution; and (4) consideration of a spectrally resolved light field [*Baird et al.*, 2007].

[10] In this work numerical experiments are undertaken with ocean state initialized with weekly mean temperature and salinity fields from 1 January 1997. Two 21-day simulations are undertaken, one forced with idealized approximately northerly alongshore winds, and a second with approximately southerly alongshore winds. The two wind patterns produce upwelling and downwelling-favorable conditions respectively. The resulting continental shelf carbon dynamics are analyzed for a study region within the model domain through the comparison of surface fields and cross-shelf sections, analysis of dynamical terms for DIC, the construction of a time-averaged carbon budget for the continental shelf and an analysis of important biological and chemical terms over time. These analyses provide a quantitative description of the transient response to wind-forced and current-driven dynamics of carbon on the continental shelf.

[11] This paper is divided into three further sections. Section 2 describes each of the circulation, biological and chemical models and their respective initial conditions and external forcings. Section 3 provides a short description of the general circulation in the simulations. This understanding is then used to interpret the biological and chemical components of the simulations. The biological and chemical responses are further analyzed by presenting the components of the carbon fluxes, a biogeochemical budget and an examination of the spatial distribution of cross-shelf fluxes. Section 4 discusses the effect of the carbon to nitrogen ratio on the air-sea gas exchange, considers the temporal-spatial evolution of upwelled filaments and their air-sea gas exchange, undertakes a sensitivity analysis of the new detrital component of the biological model, and compares the NSW shelf with other continental shelves.

2. Model Description

2.1. Ocean Circulation Model

[12] The circulation model used is the Princeton Ocean Model (POM), which has a free surface and solves the nonlinear primitive equations on a horizontal orthogonal curvilinear grid and a vertical sigma (terrain following) coordinate system using finite difference methods [*Blumberg and Mellor*, 1987]. In the POM, the variables u, v and w correspond to cross-shore (x direction), alongshore (y direction), and normal to the sigma surfaces velocity components respectively. In the southeast Australian configuration, x/y grid orientation is approximately shore normal/shore parallel everywhere. The primitive variables are solved on an Arakawa-C staggered grid such that u is computed in the center of the western boundary, v is computed in the center of the southern boundary and w and variables related to turbulent kinetic energy are computed in the center of the grid cell on the bottom face. Temperature, salinity, surface elevation and the biological variables are solved in the center point of the grid cell.

[13] The version of the POM used (*circa* 2003) includes the Craig-Banner scheme [*Craig and Banner*, 1994] for calculating the wave-driven flux of turbulent kinetic energy at the surface and a hydrostatic correction term for sigma-coordinate models [*Chu and Fan*, 2003]. The *Smagorinsky* [1963] scheme is utilized in calculating horizontal diffusion and is applied with an inverse turbulent Prandtl number (TPRNI) of 1.0 and a horizontal diffusivity coefficient (HORCON) of 0.1. Physical, biological and chemical tracers are advected using three iterations of the Smolarkiewicz upstream advection scheme [*Smolarkiewicz*, 1984]. Coastal boundary conditions are: zero normal velocity, free slip tangential velocity and zero gradient for vertical velocity, temperature and salinity.

[14] The physical configuration (Figure 1) extends along the NSW coast from 28.4°S to 37.5°S, a distance of 1025 km, and extends offshore between 395 km (at 28.4°S) and 500 km (at 37.5°S). The grid for the model has 130 cells in the cross-shore direction with a resolution between 1 and 6 km, and 325 cells in the alongshore direction with a resolution between 1.5 and 6 km. The outer six boxes on the northern, eastern and southern boundaries have smoothed coastal boundaries and bathymetries, and a tapered wind stress to reduce unwanted boundary effects.

[15] Along the eastern and southern boundaries a volume constraining radiation boundary condition with relaxation that permits oblique waves to radiate outward [*Marchesiello et al.*, 2001] is applied to elevation and the baroclinic horizontal velocity components. For the barotropic horizontal velocity components the [*Flather*, 1976] condition is applied. On the northern boundary, similar boundary conditions are applied during outflow, but during inflow are relaxed toward the initial barotropic velocity field. Temperature, salinity and the chemical and biological tracers are relaxed toward the initial condition during inflow and unaltered during outflow on the southern, northern and eastern boundaries. The western boundary is land.

[16] The vertical sigma coordinates contains 36 levels, with greater resolution in the top and bottom boundary layers. Model depth and coastline are based on a global 2-minute bathymetry produced at the Naval Research Laboratory (NRL). The minimum and maximum depths are set at 15 m and 2000 m respectively. A minimum depth of 15 m reduces numerical instability along the coastline while a maximum depth of 2000 m (rather than the actual maximum depth of >4000 m) increases the allowable time step while not significantly influencing the model results [*Oke and Middleton*, 2001]. The circulation model solves the external (barotropic) mode with a 1.7 s time step and the internal (baroclinic) mode with a 60 s time step.

2.2. Age Tracer Definition

[17] A diagnostic, time-dependent tracer 'age' [*England*, 1995; *Hall and Haine*, 2002] is used to track the movement of upwelled water. Age, τ (d), follows the equation

$$\frac{\partial \tau}{\partial t} + V \cdot \nabla \tau = \nabla \cdot (K \nabla \tau) + \Theta(z) \qquad (1)$$

where Θ (z < 90 m depth) = 1, Θ (z ≥ 90 m depth) = 0, t is time, V is the velocity of the water and K is the eddy diffusion coefficient. Age in this context is the average time a water parcel has been above 90 m, subject to diffusive and advective processes.

2.3. Light Model

[18] The light model solves for the average spectrally resolved radiation for each grid cell as determined by the processes of absorption and scattering by clear water and phytoplankton cells. The light intensity at wavelength λ at the bottom of a layer dz thick, $I_{\lambda,bot}$, is given by

$$I_{\lambda,bot} = I_{\lambda,top} e^{-K_\lambda dz} \qquad (2)$$

where $I_{\lambda,top}$ is the light intensity at wavelength λ at the top of the layer and K_λ is the vertical attenuation coefficient at wavelength λ, a result of both absorption and scattering processes. Assuming a constant attenuation rate within the layer, the average light intensity at wavelength λ, I_λ, is given by

$$I_\lambda = \frac{I_{\lambda,top} - I_{\lambda,bot}}{K_\lambda dz} \qquad (3)$$

The vertical attenuation coefficient at wavelength λ when considering absorption of chlorophyll packaged within cells and scattering, K_λ, is given by

$$K_\lambda = \frac{k_\lambda + n\overline{aA}_\lambda}{\cos\theta} \sqrt{1 + (g_1 + g_2 \cos\theta)\frac{b_{T,\lambda}}{k_\lambda + na\overline{A}_\lambda}} \qquad (4)$$

The term outside the square root quantifies the effect of packaged chlorophyll on absorption, where k_λ is the absorption due to clear water [*Baird et al.*, 2007], n is the concentration of cells, $\overline{aA}_\lambda$ is the absorption cross section of the cell and θ is the azimuth angle. The absorption cross section is calculated using geometric optics assuming a spherical cell [*Baird*, 2003]. The term within the square root represents scattering as an extended path length through the water column, where g_1 and g_2 are empirical constants and take values of 0.30 and 0.14 respectively (based on offshore, southern California values in the work of *Kirk* [1991]). The total scattering coefficient, $b_{T,\lambda} = b_{w,\lambda} + b_{phy,\lambda}\, nCV$, is the sum of scattering due to clear water, $b_{w,\lambda}$, and the product of the chlorophyll-specific phytoplankton scattering coefficient, $b_{phy,\lambda}$, and the water column chlorophyll concentration, nCV (where C is the chlorophyll concentration in the cell, and V is the cell volume). The model uses a wavelength-dependent value of $b_{w,\lambda}$ obtained from *Smith and Baker* [1981]. The value for $b_{phy,\lambda}$ is set to 0.2 (mg Chl

a m^{-2})$^{-1}$ for all wavelengths, a typical value for marine phytoplankton [*Kirk*, 1994]. For more details see the work of *Baird et al.* [2007].

[19] In the simulations solar radiation is assumed to be composed of 57 discrete wavelengths. The intensity at each discrete wavelength represents the integral of the radiation from the midpoints between bands. The wavelengths used are 340, 350,..., 790, 800, 900, 1000, 1250, 1500, 1750, 2000, 3000, 4000, 5000 and 6000 nm. The spectral grid is most resolved in the photosynthetically available wavelengths at which attenuation properties are highly variable, and less resolved in the infrared wavelengths at which attenuation properties vary smoothly. Attenuation-dependent depth-resolved heating of the water column by the spectral-resolved radiation follows *Baird et al.* [2007].

[20] The solar radiation just above the sea surface, and the azimuth angle, θ, have been calculated using orbital cycles [*Brock*, 1981] and a wavelength-dependent atmospheric transmission coefficient. The surface albedo as a function of azimuth angle is calculated using Fresnel's equation. Snell's law is used to account for the refraction of light at the air/water interface. In order to exclude a seasonal signal and the latitudinal variation in the model domain, the whole model domain is forced with a solar radiation flux that repeats the daily cycle for 1 January at 34°S for each model day and is calculated at each time step. A factor of 0.8 reduction in solar radiation has been applied equally over all wavelengths to account for the mean observed difference between clear sky solar radiation and the downward solar radiation flux for the study region during the austral summer (as determined from NCEP reanalysis [*Kalnay et al.*, 1996]). For more information on the light model, see the work of *Baird et al.* [2007].

2.4. Biological Model

[21] The biological model used is based on the pelagic lower trophic level (NPZ-type) ecosystem model of *Baird et al.* [2004]. The model of *Baird et al.* [2004] contains five state variables: dissolved-inorganic-nitrogen, or DIN (N), phytoplankton (P), zooplankton (Z), and phytoplankton reserves of nitrogen (R_N) and energy (R_I). The model of *Baird et al.* [2004] includes the processes of nutrient uptake and light capture by phytoplankton, phytoplankton growth from internal reserves, zooplankton grazing on phytoplankton and the mortality and sinking of both phytoplankton and zooplankton. Where possible, physical descriptions of the limits to ecological processes have been used. For example, the description of grazing rates of zooplankton on phytoplankton incorporates an encounter-rate calculation, based on the encounter rates of particles in a turbulent fluid, which places a maximum rate on zooplankton ingestion. The physical limits are used up until a physiological rate, such as maximum growth rate, becomes more limiting.

[22] For this study a sixth state variable, detritus (D), has been added to the biological model of *Baird et al.* [2004] (Table 1). The equations have been modified so that the phytoplankton and zooplankton mortality losses are directed into detritus, while the internal reserves of nitrogen and energy (stored as fixed carbon) of phytoplankton lost to mortality or grazing are released as DIN and DIC.

[23] The coupling of the circulation and biological models results in an advection-diffusion-reaction (ADR) equa-

Table 1. Biological and Carbon State Variables

State Variable	Symbol	Units
Dissolved inorganic nitrogen	N	mol N m^{-3}
Phytoplankton	P	mol N m^{-3}
Reserves of energy in P cell	R_I	mol photon cell^{-1}
Reserves of nitrogen in P cell	R_N	mol N cell^{-1}
Zooplankton	Z	mol N m^{-3}
Detritus	D	mol N m^{-3}
Dissolved inorganic carbon	DIC	mol C m^{-3}
Alkalinity	Alk	eq m^{-3}

tion for detrital biomass with the following dynamical terms.

$$\frac{\partial D}{\partial t} + V \cdot \nabla D = \nabla \cdot (K\nabla D) - w_D \frac{\partial D}{\partial z} + F_D \quad (5)$$

where w_D is the sinking velocity of detritus, K is the eddy diffusion coefficient, D is the concentration of detritus, V is the velocity of the water and F_D is the sink/source terms of detritus due to biological processes. The other biological state variables follow similar ADR equations, with the sinking velocities set to zero for DIN and zooplankton. The changes in each state variable due to biological processes in the modified model are given by

$$F_N = \underbrace{-k_N\left(\frac{R_N^{max} - R_N}{R_N^{max}}\right)\frac{P}{m_{P,N}}}_{\text{DIN uptake}} + \underbrace{\zeta_P R_N \frac{P}{m_{P,N}}}_{\text{regeneration}}$$
$$+ \underbrace{\left(\gamma + \frac{R_N}{m_{P,N}}\right)\min\left[\frac{\phi P}{m_{P,N}}, \frac{\mu_Z^{max}}{(1-\gamma)}\right]Z}_{\text{regeneration (due to sloppy grazing)}} + \underbrace{\zeta_D D}_{\text{decay}} \quad (6)$$

$$F_{R_N} = \underbrace{k_N\left(\frac{R_N^{max} - R_N}{R_N^{max}}\right)}_{\text{DIN uptake}} \underbrace{-\mu_P^{max}(m_{P,N} + R_N)\frac{R_N}{R_N^{max}}\frac{R_I}{R_I^{max}}}_{\text{phytoplankton growth}} \quad (7)$$

$$F_{R_I} = \underbrace{k_I\left(\frac{R_I^{max} - R_I}{R_I^{max}}\right)}_{\text{light capture}} \underbrace{-\mu_P^{max}(m_{P,I} + R_I)\frac{R_N}{R_N^{max}}\frac{R_I}{R_I^{max}}}_{\text{phytoplankton growth}} \quad (8)$$

$$F_P = \underbrace{\mu_P^{max}\frac{R_N}{R_N^{max}}\frac{R_I}{R_I^{max}}P}_{\text{phytoplankton growth}} \underbrace{-\min\left[\frac{\phi P}{m_{P,N}}, \frac{\mu_Z^{max}}{(1-\gamma)}\right]Z}_{\text{grazing}} \underbrace{-\zeta_P P}_{\text{mortality}} \quad (9)$$

$$F_Z = \underbrace{(1-\gamma)\min\left[\frac{\phi P}{m_{P,N}}, \frac{\mu_Z^{max}}{1-\gamma}\right]Z}_{\text{zooplankton growth}} \underbrace{-\zeta_Z Z}_{\text{mortality}} \quad (10)$$

$$F_D = \underbrace{+\zeta_P P + \zeta_Z Z}_{\text{mortality}} - \underbrace{\zeta_D D}_{\text{decay}} \quad (11)$$

where F_N, F_P, F_Z and F_D denotes the rate of change of DIN, phytoplankton, zooplankton and detritus measured in mol N

m^{-3} s^{-1}, F_{R_N} and F_{R_I} denotes the rate of change of the reserves of nitrogen and energy measured in mol N cell^{-1} s^{-1} and mol photon cell^{-1} s^{-1} respectively. The physical limit on nutrient uptake due to diffusion to the cell surface is given by $k_N = \psi D_N N$, where D_N is the molecular diffusivity of nitrate [*Baird et al.*, 2004] and ψ is the diffusion shape factor (Table 2). The physical limit on light capture is given by $k_I = 8.3525 \times 10^{-9} \int \overline{aA} \, I\lambda d\lambda$ mol photon cell^{-1} s^{-1}, where λ is the wavelength and $\overline{aA}_\lambda$ is the absorption cross section of the cell at λ (see section 2.3). A physical limit on grazing due to the encounter of zooplankton and phytoplankton is used. The encounter rate coefficient, ϕ, is calculated using a curvilinear formulation that includes terms for relative motion, turbulent shear and diffusion [*Jackson*, 1995; *Baird et al.*, 2004].

[24] A number of features of the phytoplankton component of the model are worth pointing out. The term $P/m_{P,N}$ which appears in the DIN uptake and the phytoplankton grazing terms, is the concentration of phytoplankton cells (referred to in section 2.3 as n). Note also that the total mass of nitrogen reserves in the model depends on both R_N and P. For comparison with the commonly used cell quota models, $m_{P,N} + R_N$ is equivalent to cellular nitrogen quota and $m_{P,N}$ is approximately equivalent to the minimum quotient. When phytoplankton grow (that is, nitrogen moves from R_N to P), the loss from R_N in equation (7) is given by the growth rate, $\mu = \mu_P^{max}\frac{R_N}{R_N^{max}}\frac{R_I}{R_I^{max}}$, multiplied by $(m_{P,N} + R_N)$, while the gain in phytoplankton biomass in equation (9) is given by the growth rate multiplied by P. Note firstly that the loss in R_N is multiplied by $m_{P,N}$ to convert the growth rate to a flux of N per cell, while the gain in phytoplankton biomass is multiplied by P to account for the change in the total phytoplankton biomass. Beyond this unit change, the greater loss in R_N than gain in P (the addition of R_N to $m_{P,N}$ in equation (7)) represents the sharing of nitrogen reserves among the now greater number of phytoplankton cells. This effect is common to all cell quota models, and is referred to as "dissipation by cell multiplication" by *Droop* [1983]. Parameter values used are described in Tables 1 and 2. For more details see the work of *Baird et al.* [2004].

2.5. Carbon Model

[25] The Ocean-Carbon Cycle Model Intercomparison Project (OCMIP) has developed numerical methods to quantify air-sea carbon fluxes and carbon dioxide system equilibria [*Najjar and Orr*, 1999]. This work uses a modified version of the OCMIP-2 Fortran code developed for MOM4 (GFDL Modular Ocean Model version 4 [*Griffies et al.*, 2004]).

[26] The state of the carbon dioxide (CO$_2$) system is quantified using two prognostic variables, the concentration of dissolved inorganic carbon, DIC, and Alkalinity, Alk. The value of these prognostic variables, along with salinity and temperature, are used to calculate the pH and partial pressure of carbon dioxide, pCO$_2$, in the surface waters using a set of governing chemical equations which are solved using a Newton-Raphson method [*Najjar and Orr*, 1999].

[27] The advection-diffusion-reaction equation for DIC is

$$\frac{\partial DIC}{\partial t} + V \cdot \nabla DIC = \nabla \cdot (K\nabla DIC) + F_{DIC} \quad (12)$$

Table 2. Parameters Used in the Biological Model[a]

	Symbol	Value	Units
Parameters independent of plankton radius			
Phytoplankton mortality	ζ_P	0.005	d^{-1}
Zooplankton mortality	ζ_Z	0.2	d^{-1}
Detrital decay rate	ζ_D	0.1	d^{-1}
Detrital sinking rate	w_D	10.0	$m\ d^{-1}$
Assimilation coefficient	γ	0.3	$-$
Redfield ratio for C to N	RED	6.625	$mol\ C\ mol\ N^{-1}$
Parameters calculated from $r_P = 1\ \mu m$, $r_Z = 20\ \mu m$			
Phytoplankton sinking rate	w_P	0.0448	$m\ d^{-1}$
Zooplankton sinking rate	w_Z	0.0	$m\ d^{-1}$
Maximum phytoplankton growth rate	μ_P^{max}	2.8	d^{-1}
Maximum zooplankton growth rate	μ_Z^{max}	1.4	d^{-1}
Phytoplankton nitrogen content	$m_{P,N}$	1.34×10^{-14}	$mol\ N\ cell^{-1}$
Zooplankton nitrogen content	$m_{Z,N}$	1.22×10^{-11}	$mol\ N\ ind^{-1}$
Phytoplankton energy content	$m_{P,I}$	8.87×10^{-13}	$mol\ photon\ cell^{-1}$
Maximum phytoplankton energy reserves	R_I^{max}	8.87×10^{-13}	$mol\ photon\ cell^{-1}$
Maximum phytoplankton N reserves	R_N^{max}	1.34×10^{-14}	$mol\ N\ cell^{-1}$
Diffusion shape factor ($4\pi r_P$)	ψ	1.26×10^{-5}	$m\ cell^{-1}$
P chlorophyll concentration	C	1.35×10^{-7}	$mg\ Chl\ m^{-3}$
Relative encounter velocity	U	310	$\mu m\ s^{-1}$

[a]Parameters based on plankton radius have been calculated from allometric relationships and geometric descriptions given in the work of *Baird et al.* [2004] using $r_P = 1\ \mu m$ and $r_Z = 20\ \mu m$. Absorption cross section $\overline{aA}_\lambda$ ($m^2\ cell^{-1}$) is a function of wavelength and is graphed in *Baird et al.* [2007, Figure 2f]. The encounter rate coefficient ϕ ($m^3\ s^{-1}\ cell^{-1}$) is a function of r_P, U, and the rate of dissipation of turbulent kinetic energy [see *Baird et al.*, 2004]. The majority of parameters with a time scale are given in units of days for ease of interpretation but are applied in the model equations with units of second.

where F_{DIC} is the change in DIC due to biological processes. There is no flux of DIC to the sediment. The surface boundary condition for DIC is given by $K_W \triangle p\text{CO}_2$ where $\triangle p\text{CO}_2$ is the difference in partial pressure of carbon dioxide between the atmosphere and the ocean. The piston velocity, K_W, for ice free regions is a function of wind speed and surface water temperature [*Najjar and Orr*, 1999; *Wanninkhof*, 1992].

$$K_W = au^2 (Sc_{\text{CO}_2}/660)^{-\frac{1}{2}} \qquad (13)$$

where u is the surface wind speed, $a = 0.337/3600\ s\ m^{-1}$ is an empirical constant, and Sc_{CO_2} is the Schmidt number for dissolved CO_2 and is given by $Sc_{\text{CO}_2} = 2073.1 - 125.62T + 3.6276T^2 - 0.043219T^3$ [*Wanninkhof*, 1992].

[28] To calculate F_{DIC} biological rates are converted from units of N to C using the Redfield ratio of RED = 6.625 mol C mol N^{-1} for marine phytoplankton [*Redfield et al.*, 1963]. Carbon is absorbed from DIC by photosynthesis, and added to the DIC pool through the breakdown of detritus and release of fixed carbon associated with the storage of energy, R_I, from the processes of phytoplankton mortality and zooplankton grazing.

$$F_{DIC} = \underbrace{-\frac{k_I}{10}\left(\frac{R_I^{max} - R_I}{R_I^{max}}\right)\frac{P}{m_{P,N}}}_{DIC\ uptake} + \underbrace{RED\zeta_D D}_{detrital\ decay} + \underbrace{RED\zeta_P P R_I / m_{P,I}}_{phytoplankton\ mortality}$$

$$\underbrace{+ RED\left(\gamma + \frac{R_I}{m_{P,I}}\right)\min\left[\frac{\phi P}{m_{P,N}}, \frac{\mu_Z^{max}}{1-\gamma}\right]Z}_{DIC\ release\ from\ zooplankton\ grazing} \qquad (14)$$

where F_{DIC} is the rate of change of DIC measured in mol C $m^{-3}\ s^{-1}$ and all other symbols used are described in section 2.4 and Tables 1 and 2. The factor of 10 in the DIC uptake

term in equation (14) has units of mol photon mol C^{-1} and converts a photon flux, k_I, into a carbon flux with a quantum efficiency slightly less than the theoretical maximum of 8. The third and fourth terms in equation (14) account for the carbon in phytoplankton reserves released directly to DIC from phytoplankton mortality and zooplankton grazing respectively. For phytoplankton mortality, $R_I/m_{P,I}$ is the ratio of DIC in reserves to that held as structural material. Multiplying this fraction by P gives the total reserves in nitrogen units. Nitrogen units are converted to carbon using RED, and the loss rate ζ_P applied to determine the flux to DIC. The grazing term includes two components. The DIC reserves of grazed phytoplankton are allocated to DIC in the same way as for phytoplankton mortality (contribution from $R_I/m_{P,I}$ term). The second component involves the allocation of the phytoplankton structural material lost due to inefficient grazing to DIC. In a model with two detrital pools (refractory and labile) this second term might be returned to a liable detrital pool. With only one pool in this model, it moves instantaneously to DIC.

[29] The equation for alkalinity, Alk, is

$$\frac{\partial Alk}{\partial t} + V \cdot \nabla Alk = \nabla \cdot (K\nabla Alk) + F_{Alk} \qquad (15)$$

where F_{Alk} is the sink/source terms for alkalinity. In the model F_{Alk} is only influenced by local changes in NO_3^- concentration, which are a function of biological processes only. As a result, $F_{Alk} = -F_N$.

2.6. Initial Conditions and Spin-up

[30] The initial conditions for DIC and alkalinity are interpolated onto the grid from the Global Oceans Data Analysis Project (GLODAP) climatology collected between 1972 and 1999 [*Key et al.*, 2004]. For the calculation of carbon dynamics, atmospheric pressure (P_a) is equal to
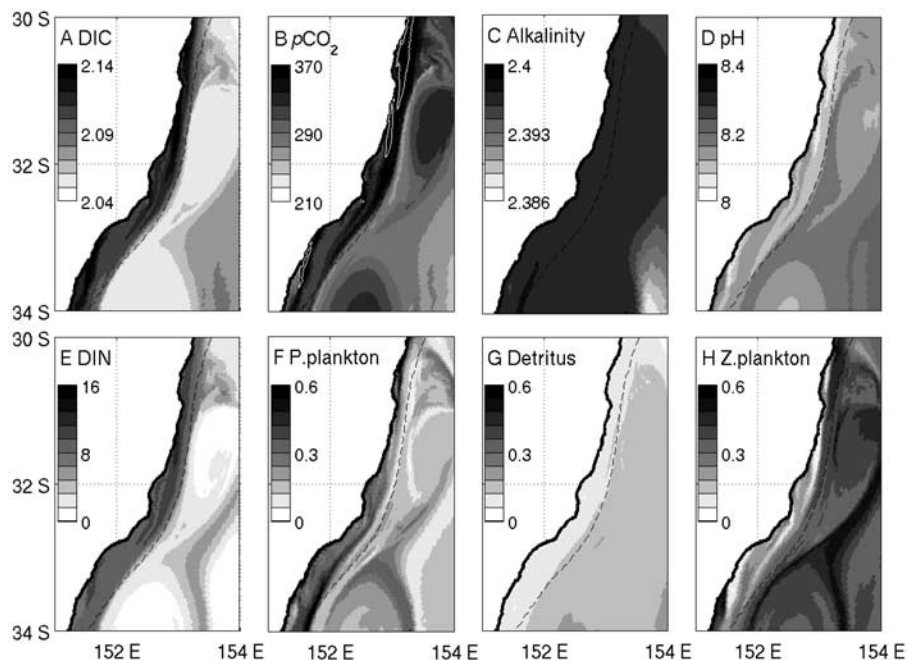
Figure 3. Surface biological and chemical properties for the upwelling wind scenario on day 20 between 30°S–34°S and 151°E–154°E. (a) DIC (mol C m^{-3}). (b) pCO$_2$ (ppmv) with a white contour for 370 ppmv (in equilibrium with the atmosphere). (c) Alkalinity (eq m^{-3}). (d) pH. (e) DIN (mmol N m^{-3}). (f) Phytoplankton (mmol N m^{-3}). (g) Detritus (mmol N m^{-3}). (h) Zooplankton (mmol N m^{-3}). The 200-m isobath is shown as a dashed line.

1 atm, and atmospheric carbon concentration (C_a) is equal to 370 ppmv. The initial conditions for phytoplankton, zooplankton and DIN are obtained from an equilibrium point in a two dimensional version of the model [*Baird et al.*, 2004]. The inflow conditions on the northern, southern and eastern boundary are set to the initial conditions. The bottom boundary condition allows for the sinking of organic matter into the sediments. Detritus is initially set to zero.

[31] The two scenarios (upwelling-favorable and downwelling-favorable winds) are initialized with temperature and salinity fields from 1 January 1997 [*Oke and Middleton*, 2001]. These fields are used to calculate the dynamic height of the water column [*Pearce*, 1983]. The initial barotropic velocities are then determined from the dynamic height. There is a two day spin-up of the physical model during which the temperature and salinity fields are held constant and the baroclinic velocity field slowly adjusts. The biological and carbon distributions are held constant for a further 2 days before being allowed to change.

[32] Two idealized simulations are run, one forced with idealised approximately northerly alongshore winds at 5 m s^{-1}, and a second with idealised approximately southerly alongshore winds at 5 m s^{-1}. The two wind patterns produce upwelling and downwelling-favorable conditions respectively (hereafter referred to as the upwelling and downwelling scenarios).

[33] The analysis in sections 3 and 4 is performed in a region extending between a northern edge at 30°S, a southern edge at 34°S, an eastern edge at 154°E and the coastline (Figure 2). The term "edge" is used for the study region so as not to be confused with the term "boundary" used for the model grid. This region has been chosen

specifically to allow an investigation of the biogeochemical dynamics in the biological important continental shelf region south the separation of the EAC.

3. Results

3.1. General Description

3.1.1. Circulation

[34] The mean sea surface temperature and surface velocity field averaged from day 10 to day 20 for the upwelling-favorable and downwelling-favorable wind scenarios are given in Figure 2. In both scenarios, the EAC is strong with currents around 1 m s^{-1}. The EAC separates from the coast near the northern edge of the study region (30°S) and flows eastwards. Two eddies form at 32°S and 34°S just offshore of the 200-m isobath. These eddies appear from day 12 and remain until the end of the simulation (not shown).

[35] In the upwelling scenario (Figure 2a), colder water has been upwelled at the coast, reducing the surface temperature by up to 4°C relative to the downwelling scenario. The surface velocity field of the upwelling scenario shows wind-driven offshelf currents, some of which are entrained into the eddy at 34°S. Just south of the EAC separation (30°S) there is a weaker current persisting along the coast. As a result, the surface flow on the continental shelf between 30°S to 34°S is generally southward and offshore with magnitudes of ∼0.1 −0.15 m s^{-1}.

[36] In the downwelling scenario (Figure 2b), the surface features of the eddies at 32°S and 34°S are better defined. The presence/absence of nutrient rich upwelled water, and the changes in the shelf current field drive differing biolog-
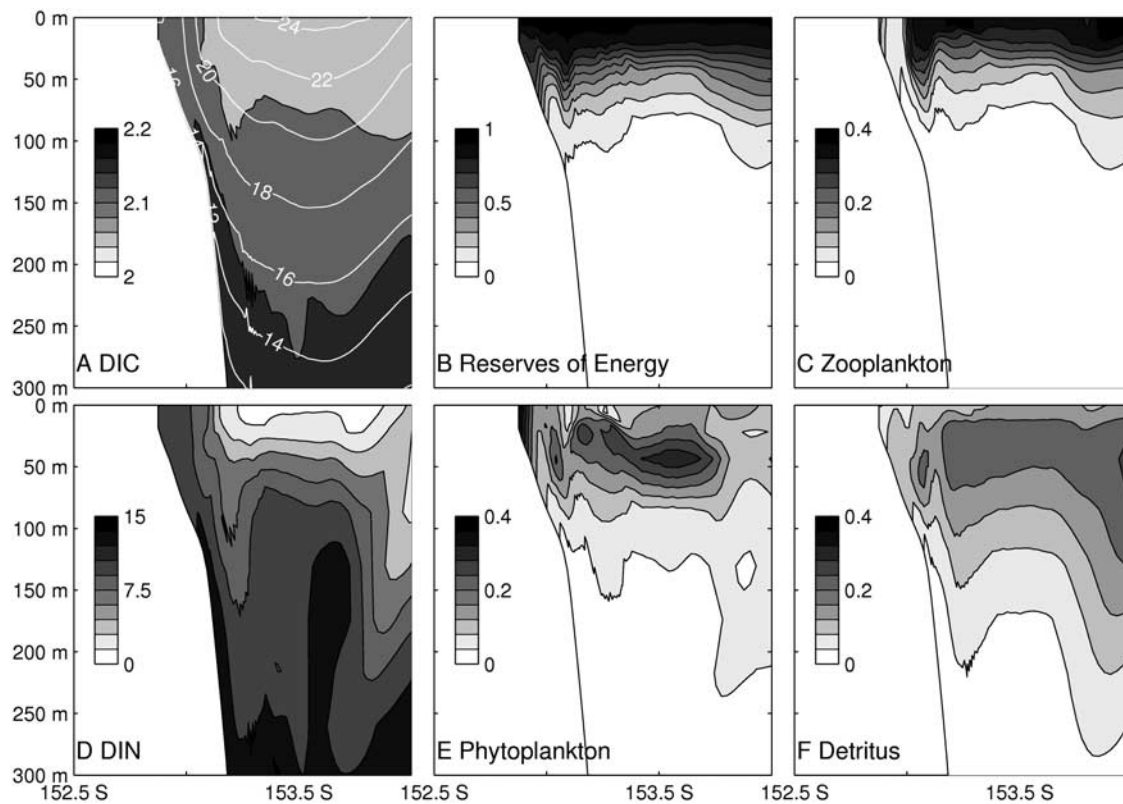
Figure 4. Cross-shelf properties at ~31°S (see Figure 1) for the upwelling wind scenario on day 20. (a) DIC (mol C m^{-3}) and temperature contours (°C). (b) Reserves of energy, R_I/R_I^{max}. (c) Zooplankton (mmol N m^{-3}). (d) DIN (mmol N m^{-3}). (e) Phytoplankton (mmol N m^{-3}). (f) Detritus (mmol N m^{-3}).

ical responses and cross-shelf carbon fluxes in the two scenarios.

3.1.2. Biological and Chemical Response

[37] On day 20 of the upwelling scenario, cool upwelled waters have reached the surface and there is an increase in surface DIC (Figures 3a and 4a) and pCO$_2$ (Figure 3b) and a decrease in pH (Figure 3d). The upwelled waters are also high in DIN (Figures 3e and 4d), which stimulates a phytoplankton bloom. The highest concentrations of phytoplankton occur on the shelf between 20 and 50 m depth (Figure 4e), with a surface increase also visible (Figure 3f). Despite consuming DIC, and therefore reducing pCO$_2$, the phytoplankton bloom at the coast does not fully offset the large increases in DIC and pCO$_2$ associated with the upwelled water. The increased DIC results in a region of surface pCO$_2$ above 370 ppmv (Figure 3b, white contour) which produces an outgassing air-sea flux. Upwelled water is generally advected south and along shelf from the initial upwelling site.

[38] Under downwelling-favorable winds, bottom Ekman transport brings DIC (Figures 5a and 6a) and DIN (Figures 5e and 6d) onto the continental shelf. This water reaches to about 50 m depth on the shelf, but it does not reach the surface (Figures 5a and 5e). As a result, there is little change in surface pCO$_2$ (Figure 5b), pH (Figure 5d), DIN (Figure 5e) or phytoplankton (Figure 5f) on the shelf.

3.2. DIC Dynamical Terms

[39] Additional simulations for the upwelling and downwelling-favorable wind scenarios have been undertaken without biological processes so as to separate the contributions that the biological and physical processes make to the carbon shelf budget.

[40] The local rate of change of DIC, or the DIC tendency, is a result of the sum of the individual processes of advection, vertical diffusion, uptake by phytoplankton (photosynthesis), regeneration of organic material through detrital decay, phytoplankton mortality and zooplankton grazing (Figures 7 and 8) and air-sea gas exchange (Figures 9 and 10).

[41] The DIC terms in the upwelling scenario on day 20 with no biological processes (Figures 7f–7j and 9j) show the effect of the upwelling of high DIC water between 30°S–34°S. The upwelled filaments that extends southward from 30°S and 31°S have a higher pCO$_2$ than the atmosphere (Figure 3b) and, as a result, lose carbon through an outgassing air-sea flux (Figure 9j). This loss produces a vertical gradient in DIC, which results in vertical diffusion supplying DIC to surface waters, and therefore a positive DIC vertical diffusion term at the surface (Figure 7h). Advection moves the front between areas of high and low DIC (Figure 3a), resulting in large local gains and losses in DIC due to advection (Figure 7g).

[42] The DIC terms in the upwelling scenario on day 20 with biology (Figures 7a–7e and 9e) can be contrasted with the no biology case (Figures 7f–7j and 9j). The most significant result is the reduced area and intensity of outgassing in the biology case (compare Figure 9e with 9j) which is a consequence of DIC uptake by phytoplankton (Figure 7d). The advective terms (Figures 7b and 7g) are
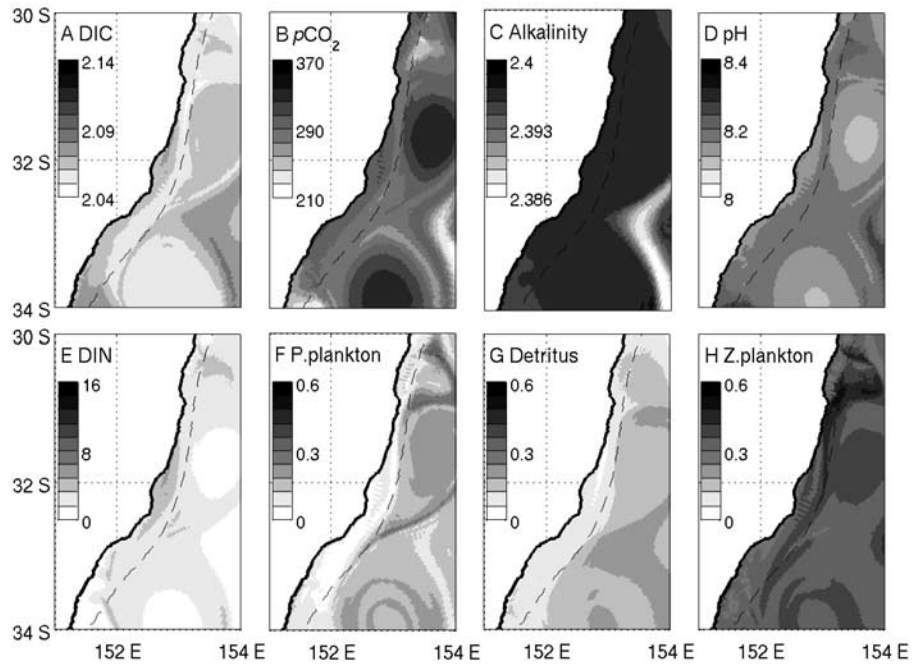
Figure 5. Surface properties for the downwelling wind scenario on day 20. For more details, see Figure 3.

almost identical as the difference between the DIC fields is small relative to their magnitude. In the continental shelf surface waters the biological terms regeneration (a gain, Figure 7e) and uptake (a loss, Figure 7d) alter the balance of DIC terms. Regeneration plus uptake is generally negative along the shelf, consuming some of the excess upwelled DIC. As a result, the air-sea flux in the case with biology is more positive (tending toward absorbing), and vertical
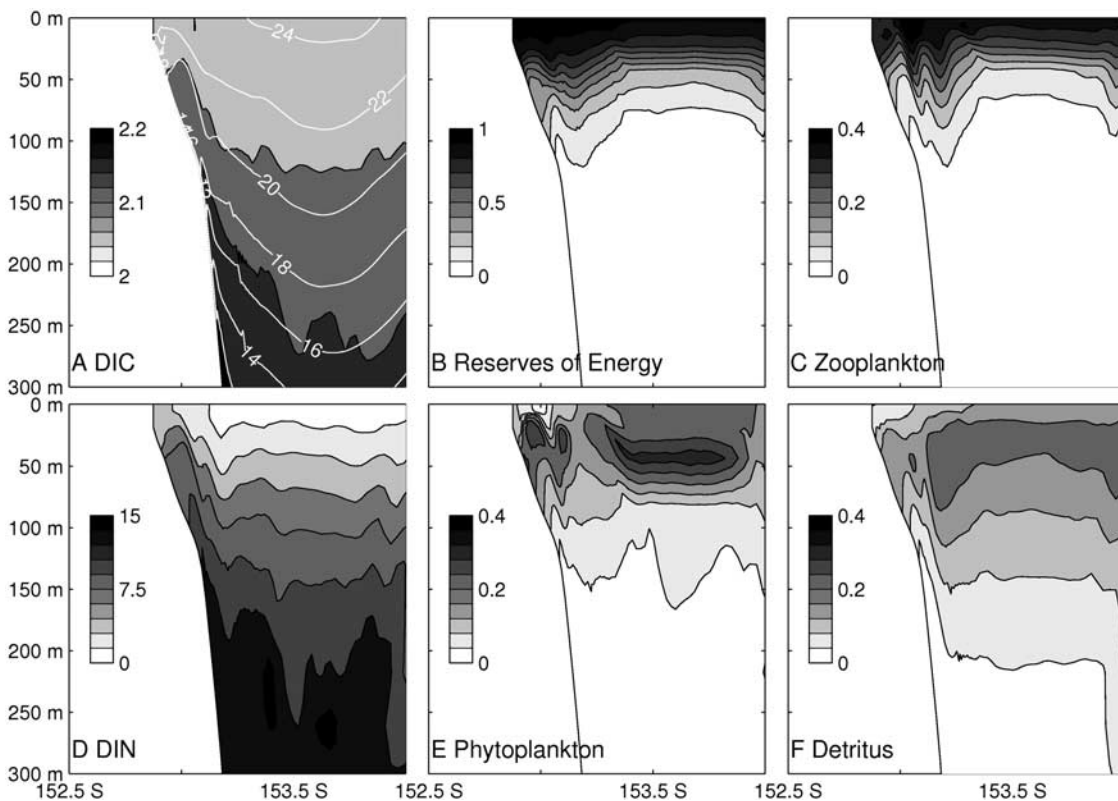
Figure 6. Cross-shelf properties at ~31°S for the downwelling wind scenario. For more details, see Figure 4.
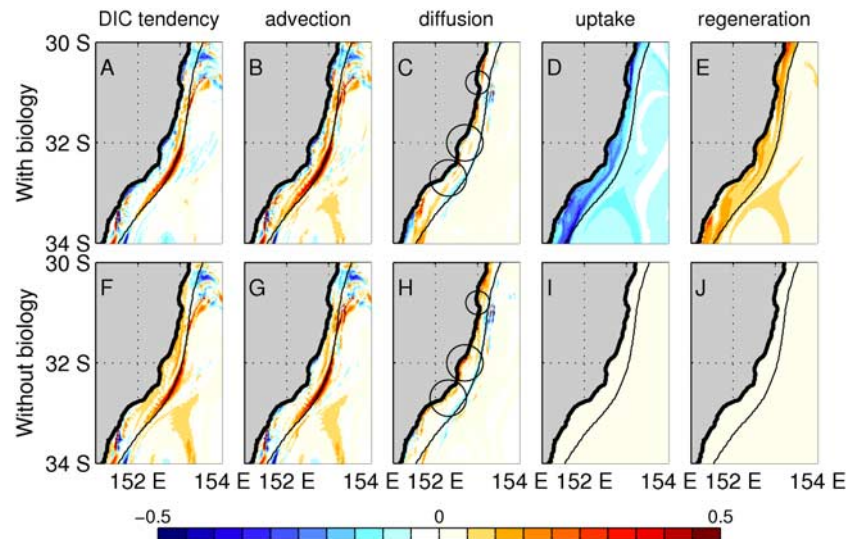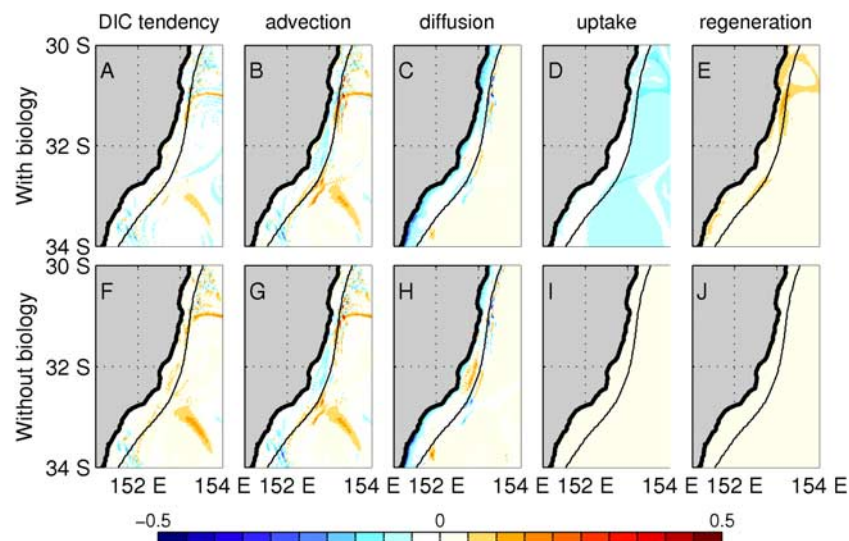
Figure 7. The contributions to the rate of change of surface DIC for the upwelling wind scenario on day 20. The contributions of (b and g) advection, (c and h) vertical diffusion, (d and i) phytoplankton uptake of DIC, and (e and j) regeneration of biological matter to the (a and f) total change in DIC. The top and bottom show model output for experiments with and without biological processes in Figures 7a–7e and Figures 7f–7j, respectively. Red indicates an increase of DIC due to the process, and blue indicates a decrease. All units are μ mol C m^{-3} s^{-1}. The 200-m isobath is drawn in black. The circles in Figures 7c and 7h indicate differences between the two cases.

diffusion more negative, with regions where the air-sea flux and vertical diffusion terms change sign. These regions correspond with filaments of a younger age which indicates upwelled water (see section 4.1; shown by circles in Figures 7c and 7h).

[43] The DIC terms in the downwelling scenario (Figures 8 and 10) have interesting differences to the upwelling scenario. The magnitude of uptake and regeneration terms on the continental shelf are generally smaller for the downwelling scenario, and therefore the difference between the biology and no biology cases is greater for the upwelling than downwelling scenario.

[44] Time evolution of the air-sea flux. At the start of the upwelling event in the upwelling scenario there are small differences between the biology and no biology cases in the air-sea gas exchange (Figures 9a and 9f). By day 14 in the upwelling wind scenario there is only a slight outgassing in the vicinity of the two upwelling sites (Figure 9b). The outgassing becomes more pronounced over time especially in the no biology case as the sum of the biological processes reduces the DIC in the water. By day 20 the no biology case has a stronger outgassing of carbon (of order of 0.01 μ mol C m^{-3} s^{-1}; Figure 9j) as biological growth has taken up extra DIC in the biology case (Figure 9e).

Figure 8. The contributions to the rate of change of surface DIC for the downwelling wind scenario on day 20. See Figure 7 for more details.
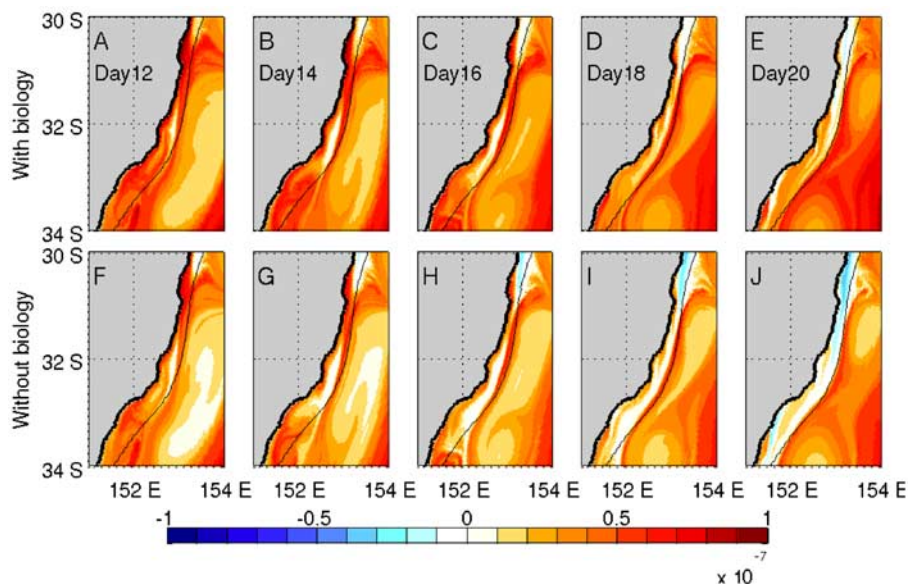
Figure 9. The air-sea gas exchange (mol C m^{-2} s^{-1}) for the upwelling scenario on (a and f) days 12, (b and g) 14, (c and h) 16, (d and i) 18, and (e and j) 20. The top is with biological process, and the bottom is without biological processes. Red indicates a flux into the ocean (absorption), and blue indicates a flux out (outgassing). The 200-m isobath is shown in black.

[45] As the deep slope water does not reach the surface in the downwelling wind scenario, outgassing of carbon does not occur. The primary productivity is also reduced (Figure 8d). As a result, while there is a slight increase in carbon uptake in the biology case, the difference between the biology and no biology cases is not as pronounced in the downwelling scenario (Figure 10).

3.3. Carbon Budget of the Continental Shelf

[46] A biogeochemical budget is calculated that quantifies the carbon held as DIC, phytoplankton, zooplankton and detritus and the fluxes for these state variables on the continental shelf from 30°S to 34°S (Figure 11). The values given in Figure 11 are time averages from day 10 to 20. Most of the carbon is in the form of DIC. There is a loss of 56 Gg C d^{-1} of DIC in the upwelling wind scenario due to biological processes (the uptake of 82 Gg C d^{-1} minus a regeneration rate of approximately 26 Gg C d^{-1}). The flux of carbon from the atmosphere (0.69 Gg C d^{-1}) is small relative to the water column physical and biological fluxes.

[47] Despite the increased phytoplankton growth in the upwelling scenario, the air-sea flux of CO_2 is less than that of the downwelling scenario. In general, upwelling in this region increases the amount of carbon stored on the conti-
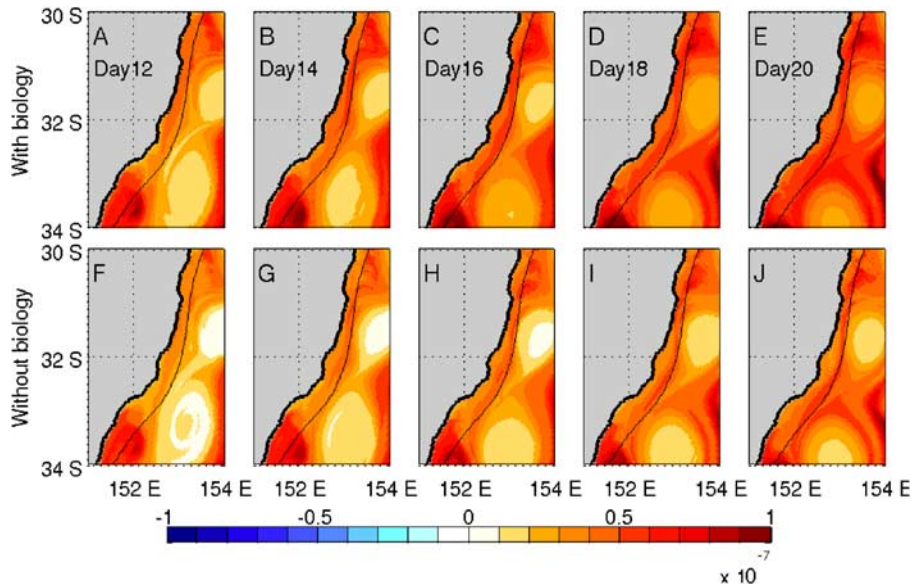
Figure 10. The air-sea gas exchange (mol C m^{-2} s^{-1}) for the downwelling scenario. For more details, see Figure 9.
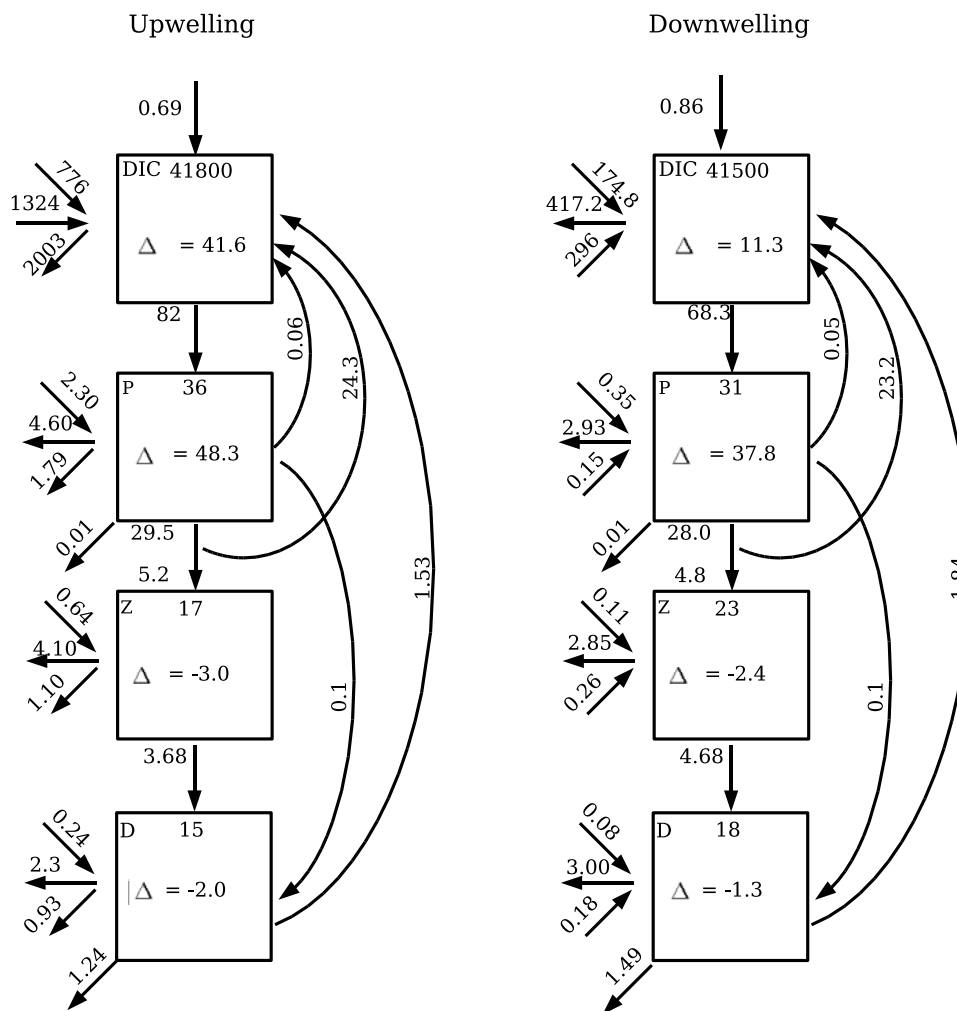
Figure 11. The depth integrated carbon shelf budget for the (left) upwelling and (right) downwelling wind scenarios averaged from day 10 to 20. Carbon components are dissolved inorganic carbon (DIC), phytoplankton (P), zooplankton (Z), and detritus (D). The carbon (Gg C) stored in each component is given at the top of each box, and the rate of change (Gg C d^{-1}) is in the center. The arrows show the direction and magnitude (Gg C d^{-1}) of the flux between the variables. The top arrow of the DIC box is the air-sea gas exchange. The arrow protruding from the bottom left corner of the P and D boxes is the sediment flux. The arrows on the left of each box represent the flux across the northern edge (top arrow), the 200-m isobath (middle arrow), and the southern edge (bottom arrow).

nental shelf as DIC. This increases the surface pCO_2, creating a greater outgassing. A detailed explanation of this finding is given in section 4.

[48] For the upwelling wind scenario there is a small flux of phytoplankton (0.01 Gg C d^{-1}) and a flux of detritus (1.24 Gg C d^{-1}) into the sediments. These values are of a similar magnitude for the downwelling wind scenario. There is a greater zooplankton biomass and less phytoplankton biomass in the downwelling wind scenario than the upwelling wind scenario.

[49] The largest difference in the DIC budget for the two wind scenarios is the fluxes of carbon entering and leaving the study region from the north, south and continental shelf edges. Both scenarios have an input of DIC at the northern edge. Because of upwelling, the water entering at the northern edge is higher in DIC in the upwelling wind scenario than the downwelling scenario (Figures 3a and

5a). There is also a greater along-shelf velocity across the north edge in the upwelling wind scenario (Figure 2a). These two factors combined lead to an over four fold increase in DIC entering the region from the northern edge in the upwelling scenario. Similarly, as there is a greater concentration of DIC in the upwelling scenario and a faster southward velocity at the south end of the domain, there is a large flux of DIC out of the region at the southern edge. The downwelling scenario has a gain of DIC at the southern edge due to a weak northward flow.

[50] The net flux of DIC due to flows through the northern and southern faces of the domain and over the 200-m isobath are just less than twice as large for the upwelling scenario (+97 Gg C d^{-1}) compared to the downwelling scenario (+54 Gg C d^{-1}). These values are of the same order of magnitude but in the opposite direction
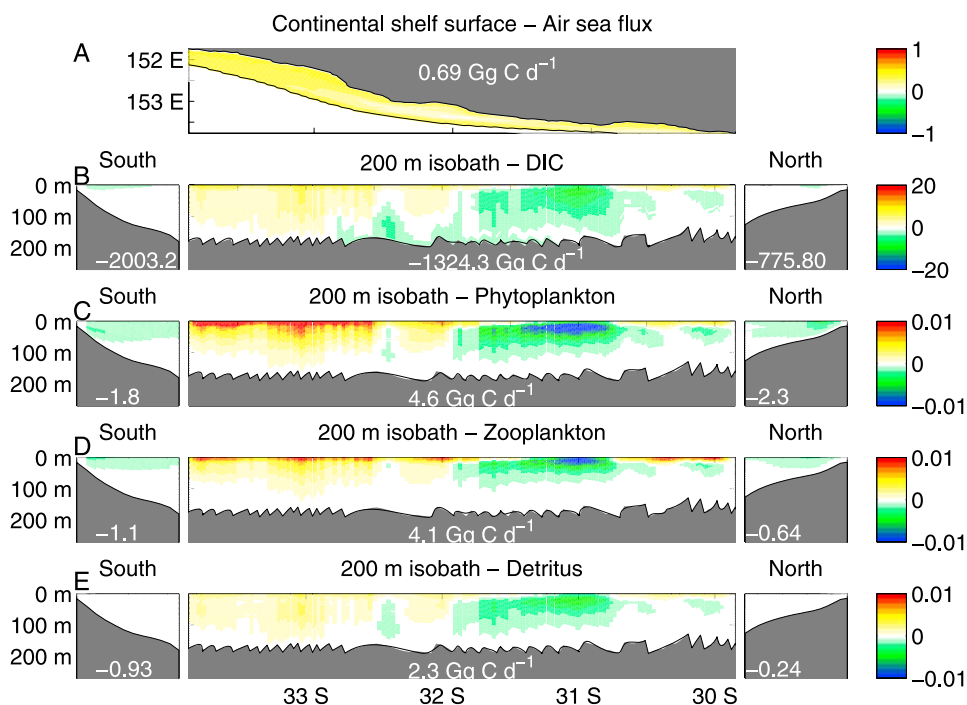
Figure 12. Spatial distribution of shelf carbon fluxes (Mg C m^{-2} d^{-1}) for the upwelling wind scenario averaged from days 10 to 20. (a) Air-Sea gas exchange and (b) DIC, (c) phytoplankton, (d) zooplankton, and (e) detrital carbon across the (left) southern edge, (middle) 200-m isobath, and the (right) northern edge. Offshelf, northward, or into the ocean are positive and shown in yellow red. Onshelf, southward, or out of the ocean are negative and shown in green blue. Total flux across the respective edges is given in each spatial distribution (Gg C d^{-1}).

as the biological processes. So while there are large fluxes through the model domain, the net is comparatively small.

[51] The net flux of carbon (a contribution from each of DIC, phytoplankton, zooplankton and detrital fluxes) in the upwelling scenario is 85 Gg C d^{-1} due primarily to upwelled DIC rich water moving onto the shelf from the continental slope. In the downwelling scenario this is reduced to 45 Gg C d^{-1}.

[52] The downwelling scenario has a loss of DIC across the 200-m isobath while the upwelling scenario has a gain due to upwelling. The upwelling scenario gains more DIC from upwelled slope water that moves across the 200-m isobath than it loses in the offshore Ekman transport. In contrast, organic carbon is lost in the surface waters in both the upwelling and downwelling scenarios due to primary production on the shelf that is advected offshore. These processes can be more readily seen in the analysis of the spatial distribution of the cross-shelf fluxes in the next section.

3.4. Spatial Distribution of Shelf Fluxes

[53] The cross-shelf fluxes of carbon are spatially heterogeneous as a result of the along-shelf variation of flows onto and off the shelf (Figures 12 and 13). The direction of the fluxes are determined by the currents (Figure 2). The upwelling-favorable scenario currents are onshelf between 31°S to 32°S, but are otherwise offshelf (Figures 12 and 2a). In contrast, the downwelling-favorable scenario currents are onshelf between 30°S to 31.2°S and 31.9°S to 32.5°S (Figures 13 and 2b). The upwelling-favorable scenario has a greater onshore flow at depth north of 32.5°S. This greater

flow at depth brings DIC-rich slope waters onto the continental shelf (Figure 12b) and is primary responsible for the change in direction of the DIC shelf flux (−1300 to 400 Gg C d^{-1}) between the two scenarios.

[54] While the spatial pattern of the direction of organic matter flux must be in the same direction as DIC (and the currents), the magnitudes vary with organic matter concentration. Each organic matter pool (phytoplankton, zooplankton and detritus) for both scenarios (Figures 12c−12e, and 13c−13e) has a net flux offshelf, due to production of organic matter on the shelf. The offshore fluxes of phytoplankton, zooplankton and detritus in the upwelling wind scenario are located primarily in the surface (Figures 12c, 12d, and 12e), while those of the downwelling wind scenario have a subsurface maximum.

[55] The spatial distribution of the air-sea flux of carbon of the two scenarios is similar north of 33°S, with the hint of a slight decrease in absorption near upwelling sites that is discussed in greater depth later. South of 33°S absorption is greater in the downwelling-favorable scenario. This occurs because cooler water flows north across the southern edge in the downwelling-favorable scenario (Figure 2b) but not in the upwelling-favorable scenario (Figure 2a). Being further from atmospheric equilibrium, a stronger absorption occurs.

4. Discussion

[56] The general model result that upwelling reduces the absorption of CO$_2$ off southeast Australia can be investi-
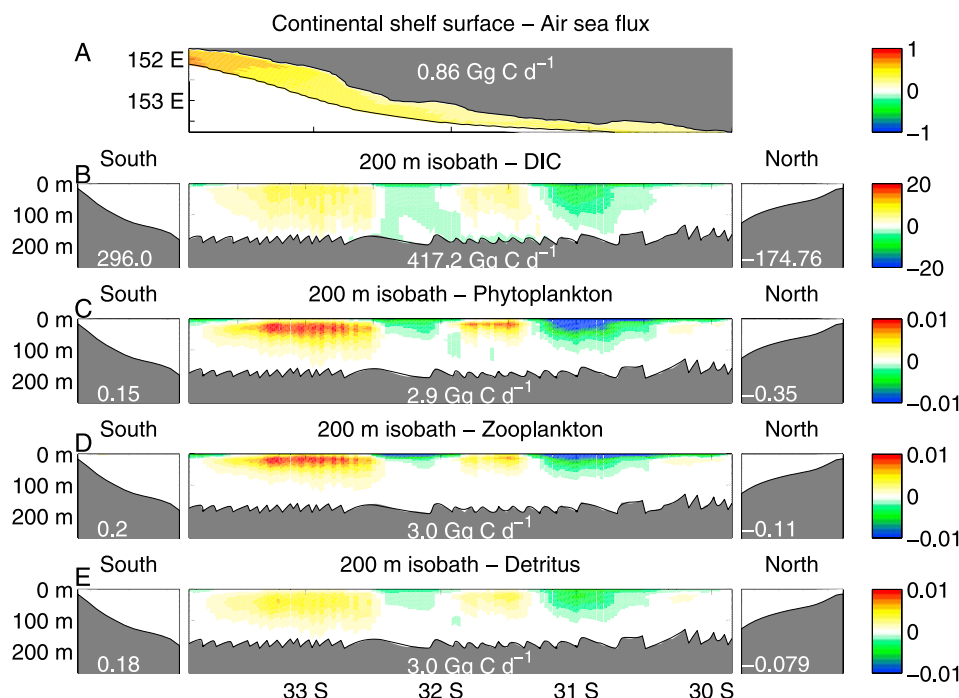
Figure 13. Spatial distribution of fluxes onto the continental shelf for the downwelling wind scenario averaged from days 10 to 20. For more details, see Figure 12.

gated further. Throughout the global ocean there is a net flux of carbon into the lower oceanic layers via sinking of detritus. Consequently, the lower oceanic layers tend to be oversaturated in DIC in comparison to what the atmospheric CO_2 concentration was at the time of the formation of the water mass [*Sarmiento and Gruber*, 2006]. As the main supply of both DIC and DIN to the surface is through upwelling, the ratio of the two in deep water will determine, to a large extent, whether upwelling results in absorption or outgassing at the sea surface.

[57] The model is initialized from a climatology [*Key et al.*, 2004] which for the region has a ratio of the gradient between the surface continental shelf to deep (500 m) ocean DIC and the gradient of the surface continental shelf to deep ocean DIN of 12.2:1 mol C:mol N. Given a Redfield carbon to nitrogen ratio for organic matter of 6.625 mol C mol N^{-1}, for every mol N upwelled, 12.2 mol C is also upwelled from which a maximum of 6.625 mol C can be consumed by primary productivity.

[58] The above calculation is complicated if the C:N ratio of phytoplankton is assumed to be variable. The biological model has a variable C:N ratio, given by $m_{P,I} + R_I{:}m_{P,N} + R_N$ (see section 2.4 and the work of *Baird et al.* [2004] for a more detailed description of the phytoplankton stoichiometry in the model). In the model surface waters from days 10 to 20, reserves of both energy (fixed carbon) and nitrogen are replete, and therefore the cellular C:N ratio is approximately Redfield. Under circumstances were C:N ratios vary significantly from Redfield, as has been shown experimentally to be possible [*Burkhardt et al.*, 1999], the above argument will need to be adjusted accordingly. For an approximately 50% increase in the C:N ratio, if all the DIN was utilized by phytoplankton, then the excess DIC would also be consumed. However, in the simulations

presented this is not the case, and the remaining fraction of carbon leads to an increase in surface DIC and pCO_2, and therefore drives the air-sea flux toward outgassing.

4.1. Carbon Fluxes in Upwelling Filaments

[59] While upwelling drives the air-sea flux of a generally absorbing region of the ocean toward outgassing, an individual parcel of upwelled water may undergo a period of outgassing followed by absorption. In order to analyze the carbon fluxes of filaments of upwelled water as they are advected offshore, a diagnostic, time-dependent tracer has been used (section 2.2). Along the coast there are several filaments of upwelled water which can be traced from their first appearance adjacent to the coast with an age of ~4 days (Figure 14a). The filaments are advected poleward and offshore and are coherent features for an additional 6 days, reaching an age of 10 days.

[60] The behavior of the air-sea gas exchange, biological uptake and regeneration within the filaments sourced from Point Plomer, Seal Rocks and Port Stephens varies with the age of the water (Figures 14b, 14c, and 14d). In general, the air-sea flux is negative (outgassing) in young waters as a result of the higher pCO_2 of recently upwelled water than the atmosphere. Within a few days the pCO_2 drops to below atmospheric levels through a combination of outgassing (Figure 14b) and phytoplankton uptake (Figure 14c) which are larger than regeneration (Figure 14d). The surface pCO_2 continues to drop through biological uptake in water with ages between 6 and 9 days, although it is slowed as the air-sea flux becomes positive (absorption). The Point Plomer filament has a stronger initial outgassing and a weaker phytoplankton uptake and regeneration than the other filaments, a result of lower phytoplankton biomass in the upwelled water (Figure 3f). A regression analysis suggests
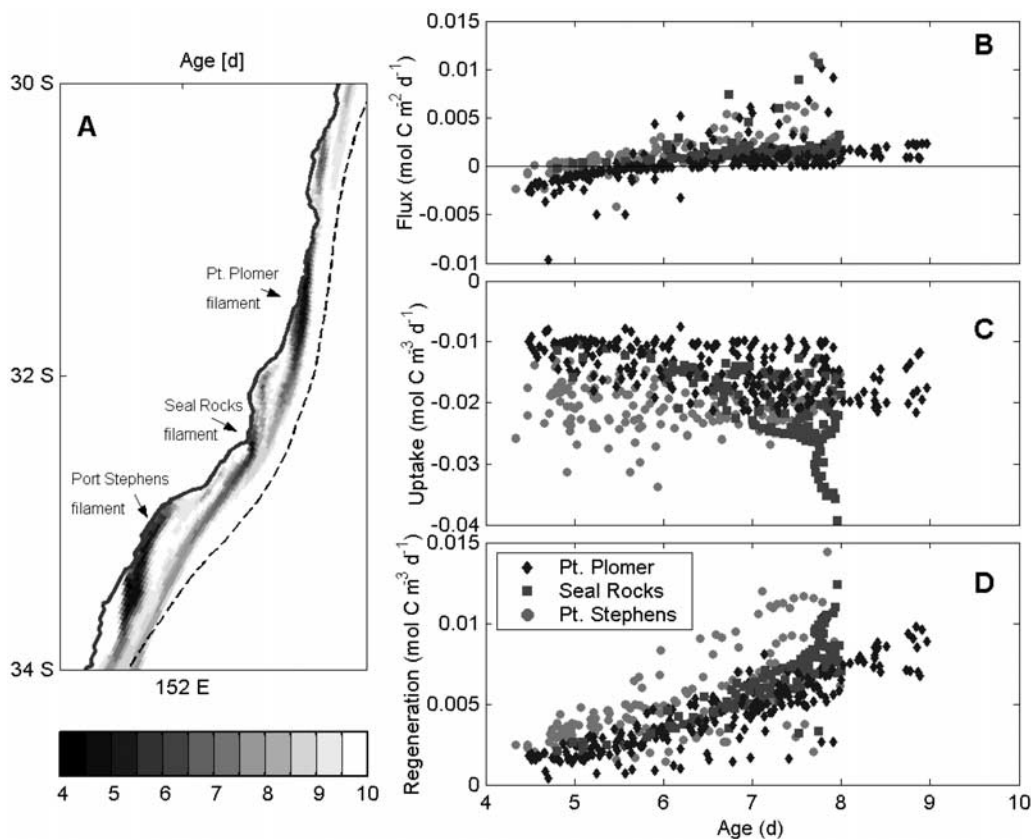
Figure 14. Spatial-Temporal trends in carbon fluxes along upwelling filaments. Figure 14a shades the age of surface water on day 20, with filaments at Point Plomer, Seal Rocks, and Port Stephens indicated. The 200-m isobath is plotted in black. A scatterplot of the age of the surface water versus (b) air-sea gas exchange (mol C m^{-2} d^{-1}), (c) phytoplankton uptake, and (d) regeneration (mol C m^{-3} d^{-1}) is shown, with symbols identifying from which of the three filaments the points are obtained.

that the surface pCO_2 of the filament at Point Plomer, which is initially greater than the atmosphere, falls to atmospheric concentrations at an age of 6 days, ~36 hours after water reaches the surface. The Seal Rocks and Port Stephens filaments reach equilibrium ~12 hours after surfacing.

4.2. Sensitivity of Continental Shelf Carbon Fluxes to Detrital Parameters

[61] Earlier work [*Baird et al.*, 2004] on the model has investigated varying the phytoplankton and zooplankton radii (and therefore a range of parameters in Table 2). A sensitivity analysis is undertaken here for the new detrital component of the model. Model carbon fluxes are sensitive to the uncertainty in the value of detrital decay and sinking rate parameters. To quantify this sensitivity, simulations have been run for a coarse resolution configuration with an idealized northerly wind of 5 m s^{-1}. The coarse resolution configuration has 82 alongshore grid cells instead of the 325 used in this paper [see *Baird et al.*, 2006a]. The sensitivity analysis involves simulations for detrital decay rates, ζ_D, of 0.05, 0.10 and 0.15 d^{-1} and detrital sinking rates, w_D, of 5, 10, and 15 m d^{-1}.

[62] The response of the detrital component is relatively linear and smooth over the nine experiments. The concentration of detritus on the continental shelf varies by a factor of 2 as ζ_D and w_D are varied by ±50% (Table 3). The highest

detrital mass on the continental shelf, 54 Gg C, is found with the lowest sinking rate and decay rate. The lowest detrital mass, 27 Gg C, is found with the highest sinking and decay rates. And, as expected, the largest decay term occurs with a slow sinking rates and fast decay rate.

[63] The water column DIC mass is three orders of magnitude larger than detritus. As a result, changing the detrital decay and sink rates does not have a large effect on the surface DIC and pCO_2. Given the small change in pCO_2, the air-sea flux of CO_2 changes by only 10% with a ±50% variation in ζ_D and w_D. There is no clear trend in the direction of the change in air-sea gas exchange with varying detrital sink and decay rates as biological feedbacks become important. Thus the uncertainties in the newly included detrital submodel do not affect the main results given in this paper on air-sea gas exchange and carbon budgets for the NSW continental shelf.

[64] For more detail results from the sensitivity analysis see the work of *Macdonald* [2007].

4.3. Comparison With Other Continental Shelves

[65] In order to understand the range of behavior of continental shelves, *Cai et al.* [2006] considered four types of ocean margins: midlatitude nonupwelling shelves, low-latitude western boundary current shelves, polar ocean margins and upwelling-dominated shelves. North of the

Table 3. Sensitivity to Detrital Parameters[a]

	Detrital Decay Rates								
	0.05	0.10	0.15	0.05	0.10	0.15	0.05	0.10	0.15
Sinking Rate	Total Shelf D			Air-Sea Flux			D Decay Term		
5	54	40	31	0.56	0.54	0.53	2.7	4.0	4.6
10	50	37	29	0.55	0.56	0.53	2.5	3.7	4.4
15	45	34	27	0.55	0.56	0.51	2.3	3.4	4.0

[a]The total amount of detritus (D) on the continental shelf (Gg C), air-sea gas exchange (Gg C d^{-1}), and detrital decay term, $\zeta_D D$ (Gg C d^{-1}) for detrital decay rates of 0.05, 0.10, and 0.15 d^{-1} and detrital sink rates of 5, 10, and 15 m d^{-1} on day 20 of the low-resolution configuration with an idealized northerly wind.

separation point of the EAC, the continental shelf behaves like a low-latitude western boundary current shelf. South of the separation point, the shelf acts more like midlatitude nonupwelling shelf. In the model scenario considered, separation occurs at ~30°S and we will restrict our discussion to the region to the south.

[66] South of the separation point in the cooler, Tasman Sea waters, the continental shelf generally acts as a sink. According to Cai's definitions [*Cai et al.*, 2006], the southern region acts like a midlatitude mesotrophic shelf such as the Baltic Sea. The continental shelf off southeast Australia is not generally upwelling favorable, like the classic upwelling regions off Chile or west Africa. However, filaments of upwelled water are common. A recent observational study of continental shelves off Iberia and NW Africa found that filaments were responsible for between 2.5 and 4.5 times the offshore carbon flux as Ekman transport [*Álvarez-Salgado et al.*, 2007]. The study further suggests that filaments are ubiquitous features in all coastal transition zone systems and must represent a significant flux of carbon to the open ocean. While filaments stand out as important features off southeast Australia (see Figure 14a) they are generally advected along the thin continental shelf and may not be lead to as large cross-shelf fluxes as found elsewhere [*Álvarez-Salgado et al.*, 2007].

5. Summary

[67] This study describes the addition of carbon chemistry and detrital components to a coupled physical-biological model to investigate carbon fluxes off southeast Australia. The Tasman Sea region is generally absorbing due to the difference in pCO$_2$ between the atmosphere and surface waters. Analysis of simulations shows that upwelling typically produces an outgassing near the site of upwelling, and absorption downstream due to carbon uptake by phytoplankton. The net result of upwelling on the continental shelf off southeast Australia is a reduced absorption of atmospheric CO$_2$.

[68] Averaged between days 10 and 20, the continental shelf between 30°S and 34°S in the upwelling scenario is a carbon gain of 85 Gg C d^{-1} due primarily to DIC and DIN rich water moving onto the shelf from the continental slope. The downwelling scenario has a reduced gain of 45 Gg C d^{-1} as less slope water is lifted onto the shelf. In contrast, the upwelling scenario absorbs 0.17 Gg C d^{-1} less atmospheric carbon than the downwelling scenario as a result of higher surface pCO$_2$. Carbon fluxes in the waters off the southeast Australian mainland are variable in space, with the transport of continental shelf waters to deep waters occurring mainly where alongshore currents separate from the coast and flow over the 200-m isobath.

References

Ajani, P., G. M. Hallegraeff, and T. Pritchard (2001), Historic overview of algal blooms in marine and estuarine waters of New South Wales, Australia, *Proc. Linn. Soc. N. S. W.*, 123, 1–22.

Álvarez-Salgado, X. A., J. Arístegui, E. D. Barton, and D. A. Hansell (2007), Contribution of upwelling filaments to offshore carbon export in the subtropical Northeast Atlantic Ocean, *Limnol. Oceanogr.*, 52, 1287–1292.

Baird, M. E. (2003), Numerical approximations of the mean absorption cross-section of a variety of randomly oriented microalgal shapes, *J. Math. Biol.*, 47, 325–336.

Baird, M. E., P. R. Oke, I. M. Suthers, and J. H. Middleton (2004), A plankton population model with bio-mechanical descriptions of biological processes in an idealised 2-D ocean basin, *J. Mar. Syst.*, 50, 199–222.

Baird, M. E., P. G. Timko, I. M. Suthers, and J. H. Middleton (2006a), Coupled physical-biological modelling study of the East Australian Current with idealised wind forcing. Part I: Biological model intercomparison, *J. Mar. Syst.*, 59, 249–270.

Baird, M. E., P. G. Timko, I. M. Suthers, and J. H. Middleton (2006b), Coupled physical-biological modelling study of the East Australian Current with idealised wind forcing. Part II: Biological dynamical analysis, *J. Mar. Syst.*, 59, 271–291.

Baird, M. E., P. G. Timko, and L. Wu (2007), The effect of packaging of chlorophyll within phytoplankton and light scattering in a coupled physical-biological ocean model, *Mar. Freshwater Res.*, 58, 966–981.

Blumberg, A. F., and G. L. Mellor (1987), A description of a three-dimensional coastal ocean circulation model, in *Three-Dimensional Coastal Ocean Models*, vol. 4, edited by N. S. Heaps, pp. 1–16, AGU, Washington D.C.

Borges, A. V., B. Delille, and M. Frankignoulle (2005), Budgeting sinks and sources of CO$_2$ in the coastal ocean: Diversity of ecosystems counts, *Geophys. Res. Lett.*, 32, L14601, doi:10.1029/2005GL023053.

Brock, T. D. (1981), Calculating solar radiation for ecological studies, *Ecol. Modell.*, 14, 1–19.

Burkhardt, S., I. Zondervan, and U. Riebesell (1999), Effect of CO$_2$ concentration on the C:N:P ratio in marine phytoplankton: A species comparison, *Limnol. Oceanogr.*, 44, 683–690.

Cai, W.-J., M. Dai, and Y. Wang (2006), Air-sea exchange of carbon dioxide in ocean margins: A province-based synthesis, *Geophys. Res. Lett.*, 33, L12603, doi:10.1029/2006GL026219.

Chu, P. C., and C. Fan (2003), Hydrostatic correction for sigma coordinate ocean models, *J. Geophys. Res.*, 108(C6), 3206, doi:10.1029/2002JC001668.

Craig, P. D., and M. L. Banner (1994), Modeling wave-enhanced turbulence in the ocean surface layer, *J. Phys. Oceanogr.*, 24(12), 2546–2559.

Droop, M. R. (1983), 25 years of algal growth kinetics: A personal view, *Bot. Mar.*, 26, 99–112.

England, M. (1995), The age of water and ventilation timescales in a global ocean model, *J. Phys. Oceanogr.*, 25(11), 2756–2777.

Flather, R. (1976), A tidal model of the northwest European continental shelf, *Mem. Soc. R. Sci. Liege*, 10(6), 141–164.

Godfrey, J. S., G. R. Cresswell, and F. M. Boland (1980), Observations of low Richardson numbers and undercurrents near a front in the East Australian Current, *J. Phys. Oceanogr.*, 10, 301–307.

Griffies, S. M., M. J. Harrison, R. C. Pacanowski, and A. Rosati (2004), A technical guide to MOM4 GFDL Ocean Group, *Tech. Rep. 5*, 342 pp., NOAA/Geophys. Fluid Dynamics Laboratory, Princeton, NJ, 3 Mar.

Hall, T., and T. Haine (2002), On ocean transport diagnostics: The idealized age tracer and the age spectrum, *J. Phys. Oceanogr.*, 32(6), 1987–1991.

Hallegraeff, G. M., and S. W. Jeffery (1993), Annually recurrent diatom blooms in spring along the NSW coast of Australia, *Aust. J. Mar. Freshwater Res.*, *44*, 325–334.

Jackson, G. A. (1995), Coagulation of marine algae, in *Aquatic Chemistry: Interfacial and Interspecies Processes*, edited by C. P. Huang, C. R. O'Melia, and J. J. Morgan, pp. 203–217, Am. Chem. Soc., Washington, D. C.

Kalnay, E., et al. (1996), The NCEP/NCAR 40-Year Reanalysis Project, *Bull. Am. Meteorol. Soc.*, *77*(3), 437–471.

Key, R. M., A. Kozyr, C. L. Sabine, K. Lee, R. Wanninkhof, J. L. Bullister, R. A. Feely, F. J. Millero, C. Mordy, and T.-H. Peng (2004), A global ocean carbon climatology: Results from Global Data Analysis Project (GLODAP), *Global Biogeochem. Cycles*, *18*, GB4031, doi:10.1029/2004GB002247.

Kirk, J. T. O. (1991), Volume scattering function, average cosines, and the underwater light field, *Limnol. Oceanogr.*, *36*, 455–467.

Kirk, J. (1994), *Light and Photosynthesis in Aquatic Ecosystems*, Cambridge Univ. Press, New York.

Macdonald, H. S. (2007), Carbon fluxes on the continental shelf off southeast Australia, Honours thesis, School of Math. and Stat., Univ. of N. S. W., Sydney, Australia. (Available at: http://web.maths.unsw.edu.au/~mbaird/Macdonald_Honours_thesis.pdf)

Marchesiello, P., J. C. McWilliams, and A. Shchepetkin (2001), Open boundary conditions for long-term integration of regional oceanic models, *Ocean Modell.*, *3*, 1–20.

McNeil, B. I., R. J. Matear, R. M. Key, J. Bullister, and J. L. Sarmiento (2003), Anthropogenic CO_2 uptake by the ocean based on the global chlorofluorocarbon data set, *Science*, *299*(5604), 235–239.

Najjar, R., and J. Orr (1999), Biotic-HOWTO. Internal OCMIP report, LSCE/CEA Saclay, Gif-sur-Yvette, France, 15 pp.

Oke, P. R., and J. H. Middleton (2001), Nutrient enrichment off Port Stephens: The role of the East Australian Current, *Cont. Shelf Res.*, *21*, 587–606.

Pearce, A. (1983), Estimation of dynamic heights from temperature profiles in the Tasman Sea, *Aust. J. Mar. Freshwater Res.*, *34*, 115–119.

Pritchard, T., P. Ajani, D. Andrew, M. Calfas, C. Holden, R. Lee, S. Linforth, and P. Rendell (1997), Relative significance of slope water, estuarine discharges and sewage outfalls for nutrients in offshore coastal waters, in *Coastal Nutrients Workshop*, pp. 44–50, Aust. Water and Wastewater Assoc., Sydney, Australia.

Redfield, A. C., B. H. Ketchum, and F. A. Richards (1963), The influence of organisms on the composition of sea-water, in *The Sea*, pp. 26–77, John Wiley, Hoboken, N. J.

Ridgway, K. R., and J. R. Dunn (2003), Mesoscale structure of the mean East Australian Current System and its relationship with topography, *Prog. Oceanogr.*, *56*, 189–222.

Roughan, M., and J. H. Middleton (2002), A comparison of observed upwelling mechanisms off the east coast of Australia, *Cont. Shelf Res.*, *22*, 2551–2572.

Roughan, M., and J. H. Middleton (2004), On the East Australia Current: Variability, encroachment, and upwelling, *J. Geophys. Res.*, *109*, C07003, doi:10.1029/2003JC001833.

Sarmiento, J. L., and N. Gruber (2006), *Ocean Biogeochemical Dynamics*, Princeton Univ. Press, Princeton, N. J.

Shim, J. H., D. Kim, Y. C. Kang, J. H. Lee, S.-T. Jang, and C.-H. Kim (2007), Seasonal variations in pCO_2 and its controlling factors in surface seawater of the northern East China Sea, *Cont. Shelf Res.*, *27*, 2623–2636.

Smagorinsky, J. (1963), General circulation experiments with the primitive equations. I. The basic experiment, *Mon. Weather Rev.*, *91*, 99–164.

Smith, R. C., and K. S. Baker (1981), Optical properties of the clearest natural waters, *Appl. Optics*, *20*, 177–184.

Smolarkiewicz, P. K. (1984), A fully multidimensional positive definite advection transport algorithm with small implicit diffusion, *J. Comput. Phys.*, *54*, 325–362.

Takahashi, T., et al. (2002), Global sea-air CO_2 flux based on climatological surface ocean pCO_2, and seasonal biological and temperature effects, *Deep Sea Res. Part II*, *49*, 1601–1622.

Tsunogai, S., S. Watanabe, and T. Sato (1999), Is there a "continental shelf pump" for the absorption of atmospheric CO_2, *Tellus*, *51B*, 701–702.

Wanninkhof, R. (1992), Relationship between wind speed and gas exchange over the ocean, *J. Geophys. Res.*, *97*(C5), 7373–7382.

Yool, A., and M. J. R. Fasham (2001), An examination of the "continental shelf pump" in an open ocean general circulation model, *Global Biogeochem. Cycles*, *15*(4), 831–844.

————————————

M. E. Baird, H. S. Macdonald, and J. H. Middleton, Climate and Environmental Dynamics Laboratory, School of Mathematics and Statistics, University of New South Wales, Sydney, NSW 2052, Australia. (s3132302@science.unsw.edu.au)